Journal of Materials Research and Technology 41 (2026) 4204–4215

Contents lists available at ScienceDirect

Journal of Materials Research and Technology

journal homepage: www.elsevier.com/locate/jmrt

# Anisotropy limitations in additive manufacturing with material extrusion

Benjamin Podmiljšak *, Matej Komelj, Anubhav Vishwakarma, Petra Jenuš, Sašo Šturm, Kristina Žužek

*Department for Nanostructured Materials, Jožef Stefan Institute, Jamova cesta 39, 1000, Ljubljana, Slovenia*

A B S T R A C T

Achieving anisotropy in additively manufactured composites is essential for high-performance functional materials but remains challenging in fused filament fabrication (FFF). This study investigates a field-assisted FFF approach using strontium hexaferrite ($SrFe_{12}O_{19}$)–polyphenylene sulfide (PPS) composites, in which particle alignment is induced by processing on top of a high-strength neodymium–iron–boron (Nd–Fe–B) magnet. Two configurations were compared: (i) a continuous setup, where the growing printed material remains in direct contact with the magnet and can act as a flux-guiding core, and (ii) a spacer-based setup, where non-magnetic spacers separate the print from the field source.

Structural, functional (magnetic) measurements and finite element simulations (FEMM) were used to quantify the evolution of anisotropy as a function of build height. In the continuous configuration, particle alignment—and thus macroscopic anisotropy—remains high up to about 20 mm, with $\langle cos\,\theta \rangle$ 0.90, and then gradually declines while still being detectable at 57.5 mm. Spacer-printed samples lose anisotropy much earlier, with $\langle cos\,\theta \rangle$ approaching isotropic values (~0.5) beyond 20–25 mm. Simulations reproduce these trends and show that previously deposited material acts as a flux-guiding path, sustaining a predominantly uniaxial field with height.

The results define practical limits for static-field alignment in material-extrusion processing and provide geometry-dependent design rules for scalable fabrication of anisotropic ceramic–polymer composites. The findings are relevant for materials and process design in applications where controlled anisotropy is required over centimetre-scale dimensions.

## 1. Introduction

Hard magnetic materials, including neodymium-iron-boron (Nd-Fe-B) or samarium-cobalt (Sm–Co) alloys, and hard ferrites ($BaFe_{12}O_{19}$ or $SrFe_{12}O_{19}$), are critical components in a wide range of applications such as motors, sensors, actuators, and generators—due to their high coercivity, remanent magnetization, and energy density [1–3]. Traditionally, these materials are manufactured using well-established techniques like powder metallurgy, sintering, and injection molding. While these methods produce high-performance magnets, they are limited in terms of design flexibility and often require extensive post-processing, such as machining to achieve complex geometries.

In recent years, additive manufacturing (AM), commonly referred to as 3D printing, has advanced beyond plastics and metals to encompass complex magnetic composites and alloys [4]. The term "3D-printed magnets" typically refers to magnets fabricated using techniques such as:

- **Binder Jetting:** Magnetic powder is selectively deposited and bound layer-by-layer [5,6].
- **Selective Laser Sintering/Melting (SLS/SLM):** Magnetic powder layers are fused using a laser to create a dense structure [7–14].
- **Stereolithography:** Magnetic powders are cured within a photosensitive resin [15–17].
- **Fused Filament Fabrication (FFF/FDM):** Magnetic powders are combined with a polymer binder, extruded as filament, and deposited layer by layer [18–24].
- **Inkjet Printing/Material Jetting:** Magnetic inks are precisely deposited and then cured [25].

These techniques provide significant benefits, including the ability to fabricate magnets with intricate geometries, internal structures, and material gradients. This flexibility can improve device performance, reduce material waste, enable rapid prototyping, and allow on-demand manufacturing of customized or low-volume parts. However, no method is without its limitations.

Despite its potential, several challenges must be overcome for AM to become commercially viable for magnetic materials. These include:

- Reduced magnetic performance due to limited control over microstructure and composition

* Corresponding author.
*E-mail address:* benjamin.podmiljsak@ijs.si (B. Podmiljšak).

https://doi.org/10.1016/j.jmrt.2026.02.041
Received 29 November 2025; Received in revised form 3 February 2026; Accepted 4 February 2026
Available online 5 February 2026

- Thermal and mechanical stresses introduced during printing and post-processing
- Stringent requirements for powder quality and feedstock preparation
- The gap between laboratory demonstrations and industrial-scale implementation

Another major obstacle explored in this paper is the inefficient alignment of magnetic particles. The alignment of particles, particularly for magnetically anisotropic materials, plays a pivotal role in determining the magnetic performance of fabricated magnets. When magnetic particles are uniformly oriented with their easy magnetization axes aligned, the resulting material can exhibit significantly enhanced properties such as higher remanent magnetization and maximum energy product $(BH)_{max}$. This directional dependence of magnetic behavior—known as magnetic anisotropy—is crucial for maximizing the efficiency and functionality of permanent magnets in various applications, ranging from electric motors to medical devices. Therefore, achieving precise particle alignment during fabrication, especially in additive manufacturing (AM) contexts, is vital to unlocking the full potential of high-performance magnetic materials.

In traditional manufacturing, magnetically anisotropic magnets are often aligned using strong magnetic fields, which is particularly important for Nd–Fe–B-based materials for assuring the high remanent magnetization and the maximum energy product $(BH)_{max}$ [26]. Replicating this magnetic moment alignment in 3D-printed magnets—either *in-situ* or post-process—remains a significant challenge.

To date, many AM-fabricated magnets are magnetically isotropic or only weakly anisotropic, often offering reduced magnetic performance due to limited control over particle orientation. While extrusion-based processes can induce a certain degree of flow-induced anisotropy—particularly in composites containing non-spherical particles such as strontium ferrite platelets—this anisotropy is generally weaker and less controllable than that achieved through field-assisted alignment. A key innovation lies in enabling magnetic anisotropy at the microstructural level. This can be achieved either through the use of single-crystalline particles—each possessing a well-defined easy magnetization axis—or through oriented polycrystalline or agglomerated particles, such as those produced by techniques like hydrogenation–disproportionation–desorption–recombination (HDDR) in the case of Nd–Fe–B-based materials. These materials can exhibit collective anisotropic behavior if their crystallites are preferentially aligned. Under an external magnetic field, each particle experiences a torque that tends to align its easy magnetization axis with the field direction. This interaction is governed by magnetocrystalline-anisotropy energy, demagnetizing energy (including shape anisotropy), exchange energy, and the Zeeman energy due to the coupling with an external magnetic field. In fused filament fabrication, in the absence of shape anisotropy, the magnetic torque aligns the particle's easy axis parallel to the field, while the molten polymer's viscosity and friction counteract this effect. Sarkar et al. proposed a model for these coupled particle-fluid-field interactions. They describe how magnetic particles interact with both the polymer matrix (fluid) and an external magnetic field during FFF printing. The goal is to understand and predict the degree to which these particles can be aligned to create anisotropic magnetic properties in the final printed object. Their model accounts for the magnetic torque acting on anisotropic particles, the viscous drag imposed by the polymer melt, and the transient thermal and flow conditions during extrusion [27,28]. It yields an estimate of the degree of alignment (DoA) by balancing these forces over the particle's rotational dynamics, helping to optimize printing conditions such as magnetic field strength, nozzle temperature, and extrusion speed to maximize magnetic anisotropy in the printed part. However, the model is limited by several simplifying assumptions, such as neglecting interparticle interactions, complex flow geometries inside the nozzle, and the statistical distribution of particle shapes and orientations, which may become significant in highly filled or large-volume prints.

Strontium hexaferrites ($SrFe_{12}O_{19}$) offer a particularly attractive platform for investigating anisotropic 3D-printed magnets. Their moderate coercivity and ability to orient at lower magnetic field strengths make them especially amenable to alignment strategies that are impractical for rare-earth-based systems. As a result, they serve as an ideal testbed for developing and refining magnetic-alignment techniques in additive manufacturing. One effective approach involves a dual mechanism: applying a static magnetic field using a permanent magnet beneath the build platform and simultaneously exploiting the natural flow-induced orientation that occurs during fused filament fabrication (FFF). This synergy enhances particle alignment during deposition. Results of magnetic measurements confirmed a notable increase in remanence—clear evidence of successful anisotropy—when compared to isotropic control samples [18,29].

Another technique involves post-printing exposure to a magnetic field at elevated temperatures to enable particle alignment. For example, aligning a Nd-Fe-B/Sm-Fe-N Nylon composite with 65 vol% magnetic filler in a 1590 kA/m field produced magnets with a $(BH)_{max}$ of up to 90 kJ/m$^3$, though the process often induced geometric distortions due to the proximity of the texturing temperature to the polymer's melting point [30].

Podmiljšak et al. successfully fabricated polyphenylene sulfide-based Sr-based hexaferrite bonded magnets using an unmodified commercial printer, suitable for high-temperature applications (up to 200 °C). Due to high porosity at 90 wt% loading, the composition was reduced to 70 wt% of loading, resulting in lower density but alignment of more than 90% of the particles up to 4 mm in height. Alignment was achieved by printing directly on a high-energy Nd-Fe-B magnet [20]. Suppan et al. developed a more sophisticated system to produce perpendicular alignment fields, but large magnetic fields attracted particles to the magnet poles, preventing printability. This restricts the method's usability to low-field applications, such as ferrites, and not rare-earth magnets. In their setup, they used permanent $Sm_2Co_{17}$ magnets positioned close to the printer nozzle to generate the alignment field. Although these magnets can create strong magnetic fields, their use with highly magnetic particles—such as $Sm_2Fe_{17}N_3$ or Nd-Fe-B—causes severe particle agglomeration at the magnet poles, clogging the printing path and disrupting extrusion. This effect was not observed with lower-magnetization fillers like $SrFe_{12}O_{19}$ ferrite, which aligned well under the same field without disrupting the process. Therefore, the technique is limited to low-saturation materials that are less responsive to magnetic attraction, restricting its applicability to ferrite-based composites. The authors noted that using an electromagnet could offer better control over the field strength and switching but was not implemented in their current study [31].

Powder-based AM techniques like Laser Powder Bed Fusion (LPBF) remain largely underexplored. Mapley et al. integrated Helmholtz coils into the powder bed to align a 60 vol% Nd-Fe-B feedstock composed of anisotropic MQP-S-11-9 Nd-Fe-B powder and a 40 vol% thermoplastic binder, forming a bonded magnetic composite. However, the applied magnetic field displaced particles and caused voids, resulting in 57% porosity [11].

Schäfer et al. introduced a single-step LPBF method using mechanically aligned Nd-Fe-B particles in a polyamide-12 matrix, eliminating the need for an external magnetic field. They employed mechanical alignment through shear torque exerted by the recoater blade during powder spreading, which oriented the ellipsoidal particles via shape anisotropy. The Nd-Fe-B powder used was an anisotropic grade (MQA-38-14), produced by pulverizing hot-deformed magnets to retain strong crystallographic alignment. Their approach achieved an alignment factor ($\langle cos\ \theta \rangle$) of up to 0.78, yielding remanence values up to 377 mT and energy products of 28.6 kJ/m$^3$ [32].

Binder Jetting also presents challenges, as aligned powder can interfere with the printhead. Li et al. used Binder Jetting to fabricate near-net-shape bonded magnets using MQP-B+ isotropic Nd-Fe-B powder (from Magnequench), composed of spherical, pre-alloyed particles.

After printing, a thermosetting epoxy binder was infiltrated into the part and cured. To improve magnetic alignment and performance, a magnetic field was applied during the curing process by placing a magnet beneath the print, resulting in a significant increase in energy product from 19.1 kJ/m$^3$ to 30.2 kJ/m$^3$ [5].

These studies illustrate that various methods—magnetic or mechanical—have been explored to induce magnetic anisotropy in printed parts. However, integrating strong magnetic fields into a printer is technically demanding, especially for rare-earth-based magnets, due to increased equipment size and complexity. For instance, in the study by Li et al. [2], the printed magnets were relatively small, typically on the order of a few cubic centimeters, which allowed for effective field alignment using a permanent magnet during curing. Similarly, other studies investigating field-assisted alignment have generally used compact samples, often limited to less than 10 cm$^3$ in volume. Consequently, most research has focused on small parts; the influence of external magnetic fields on larger printed structures remains poorly understood.

This study investigates the extent to which an external magnetic field produced by a permanent magnet can continue to serve as an effective alignment mechanism as the printing height increases. Importantly, it also explores how the printed underlying composite structure—i.e., the already-printed material—may influence the orientation of subsequently deposited particles. Since magnetic field strength decays rapidly with distance from the source and becomes increasingly inhomogeneous, it is hypothesized that the printed part itself, acting similarly to a flux conduit—analogous to a core in an electromagnetic device—could locally concentrate and direct the field. To evaluate this, samples were printed in two configurations: one directly on top of a permanent magnet continuously, and the other separated by non-magnetic spacers. This comparison aims to quantify the extent to which the presence of a printed core-like structure enhances field alignment in the upper layers of the print.

The findings have practical implications beyond magnet design, as they address a general question in field-assisted processing of anisotropic composites: over what length scale can a base-applied field effectively generate and maintain anisotropy in a growing part, and how does the part's own geometry and material response feed back into the field distribution? By combining structural, functional and numerical analysis, the present work maps the processing–microstructure–property relationships and establishes geometry-dependent design rules for field-assisted material-extrusion processing of anisotropic ceramic–polymer composites.

## 2. Materials and methods

### 2.1. Materials and filament preparation

Composite filaments were prepared from commercially sourced $SrFe_{12}O_{19}$ powder (nominal purity 99 %) and polyphenylene sulfide (PPS) in a 70:30 wt% ratio. This composition corresponds to a nominal $SrFe_{12}O_{19}$ filler fraction of approximately 38 vol% based on bulk material densities, as reported previously for $SrFe_{12}O_{19}$–PPS composites [20]. The strontium ferrite exhibited a bimodal particle size distribution, with smaller particles in the 200–500 nm range and larger particles between 1 and 5 μm. The PPS grade was chosen for its suitability in high-temperature applications and plastomagnet production.

Prior to compounding, PPS was dried for 4 h at 130 °C in a dry-air ventilated oven. Mixing and extrusion were performed using a twin-screw co-rotating extruder (PolyLab HAAKE Rheomex PTW 16, Thermo Haake, Germany) fitted with a 2.85 mm die. Eleven heating zones were configured to achieve a melt temperature of approximately 300 °C at the nozzle. Each material batch was extruded twice to enhance homogeneity.

The filament formulation, compounding strategy, and extrusion parameters follow a previously established processing route for $SrFe_{12}O_{19}$–PPS composites, which was shown to provide stable extrusion and homogeneous particle dispersion in material-extrusion additive manufacturing [20].

### 2.2. Fused filament fabrication and printing configurations

Cylindrical specimens with a nominal diameter of 10 mm were fabricated using a Hage 140L fused filament fabrication (FFF) 3D printer. Filaments with a diameter of 2.75 mm were printed through a 0.4 mm nozzle. To reduce macroporosity and improve interlayer bonding, an extrusion multiplier of 1.19 was applied, resulting in slight over-extrusion. The main printing parameters were kept constant for all samples: layer height 0.15 mm, print speed 10 mm s$^{-1}$, nozzle temperature 335 °C, and build-plate temperature 90 °C.

To induce particle alignment during printing, a static magnetic field was applied using a Nd–Fe–B permanent magnet positioned beneath the build platform. Two distinct printing configurations were employed, schematically illustrated in Fig. 1, which also defines the sample segmentation and height designations used throughout this work.

The correspondence between continuous-print segments and spacer-based samples at matching centre heights is summarized in Table 1.

#### 2.2.1. Continuous printing on a magnet

In the continuous configuration (Fig. 1a), a Nd–Fe–B permanent magnet was placed directly beneath the print bed, producing a predominantly vertical magnetic field component of approximately 390 mT at nozzle level, while horizontal components remained below 20 mT. As the part was grown layer-by-layer, the already deposited material was continuously exposed to the magnetic field and could act as a flux-guiding path.

In this configuration, a single 60 mm high cylindrical sample was printed and subsequently cut into twelve segments of equal height (5 mm) for local characterization. The segments were labelled by the height of their centre above the magnet surface, ranging from 2.5 mm to 57.5 mm.

#### 2.2.2. Spacer-based printing

In the spacer-based configuration (Fig. 1b), non-magnetic aluminium spacers with discrete heights ($h_i$) were inserted between the magnet and the print bed. This increased the distance between the deposited material and the magnetic field source, simulating conditions without a magnetic core and leading to a faster decay of the vertical magnetic field component with height.

Separate cylindrical samples were printed on spacers with heights chosen to match the centre positions of the corresponding segments in the continuous-print sample. Heating coils were integrated into the spacer platform to maintain a consistent build-plate temperature for all prints.

Photographs of the two printing configurations are shown in Fig. 2.

### 2.3. Microstructural characterization

Microstructural analysis was performed by scanning electron microscopy (SEM) using a Thermo Fisher Quanta 650 ESEM microscope. For the continuous configuration, samples were taken from three representative heights: near the base (closest to the magnet), the middle, and the top. Spacer-based samples were selected at matching heights $h_i$.

All samples were sectioned and metallographically polished using isopropanol-based diamond suspensions, first with 3 μm and then with 0.25 μm paste, to reveal particle orientation and distribution. The orientation of the hexagonal $SrFe_{12}O_{19}$ platelets relative to the build direction and external field was evaluated qualitatively from SEM images.

All samples were sectioned in a plane perpendicular to the build (z) direction, such that the observed cross-sections correspond to x–y planes at defined heights along the printed cylinder. For each configuration,

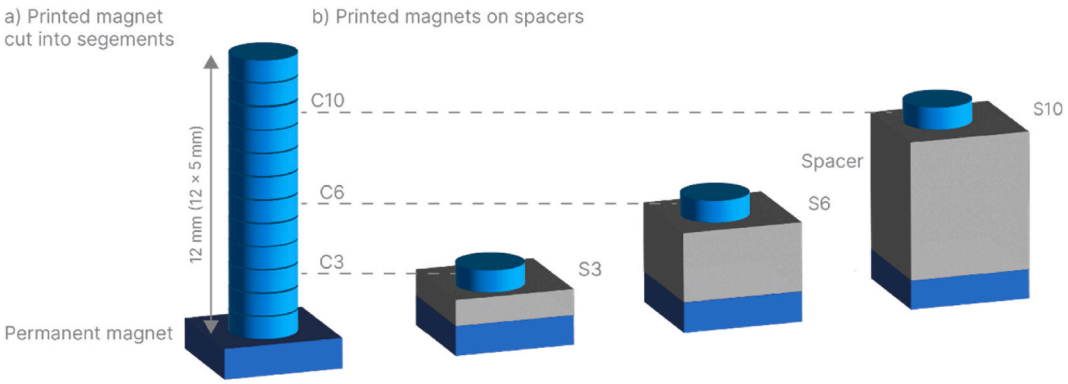


**Fig. 1.** Schematic illustration of the two printing configurations and sample identification scheme used in this study. (a) Continuous-print configuration, where a single cylindrical sample is printed directly on the Nd–Fe–B permanent magnet and subsequently sectioned into segments $C_i$, each defined by the height of its centre ($h_i$) above the magnet surface. (b) Spacer-based configuration, where individual samples $S_i$ are printed on non-magnetic aluminium spacers. Spacer block heights are selected such that the centre of each printed sample corresponds to the same centre height $h_i$ as the respective $C_i$ segment. Only the sample identification ($C_i$, $S_i$) are indicated; spacer block heights are omitted for clarity.

**Table 1**
Sample identification and centre heights.

| Index $i$ | Continuous sample | Spacer sample | Centre height $h_i$ (mm) |
|---|---|---|---|
| 1 | C1 | S1 | 2.5 |
| 2 | C2 | S2 | 7.5 |
| 3 | C3 | S3 | 12.5 |
| … | … | … | … |
| 12 | C12 | S12 | 57.5 |

representative samples from selected heights were analyzed.

The term "qualitative evaluation" refers to visual assessment of platelet orientation and alignment trends based on the angular distribution and aspect ratio of $SrFe_{12}O_{19}$ platelets observed in SEM images, rather than image-based statistical texture analysis.

SEM images were acquired at magnifications up to 135 ×, as shown in Fig. 6, which was selected to visualize particle orientation and mesoscale structural anisotropy across the printed cross-sections.

### 2.4. Magnetic measurements and alignment quantification

Magnetic measurements were carried out using a vibrating sample magnetometer (VSM, Lakeshore). Prior to measurement, each sample was magnetized in a pulsed field of 6 T to ensure full saturation.

To assess anisotropy, hysteresis loops were recorded in two orthogonal directions: parallel (0°) and perpendicular (90°) to the printing/field direction, corresponding to the easy and hard measurement axes, respectively. From these loops, remanent magnetization values $M_{r,0}$ and

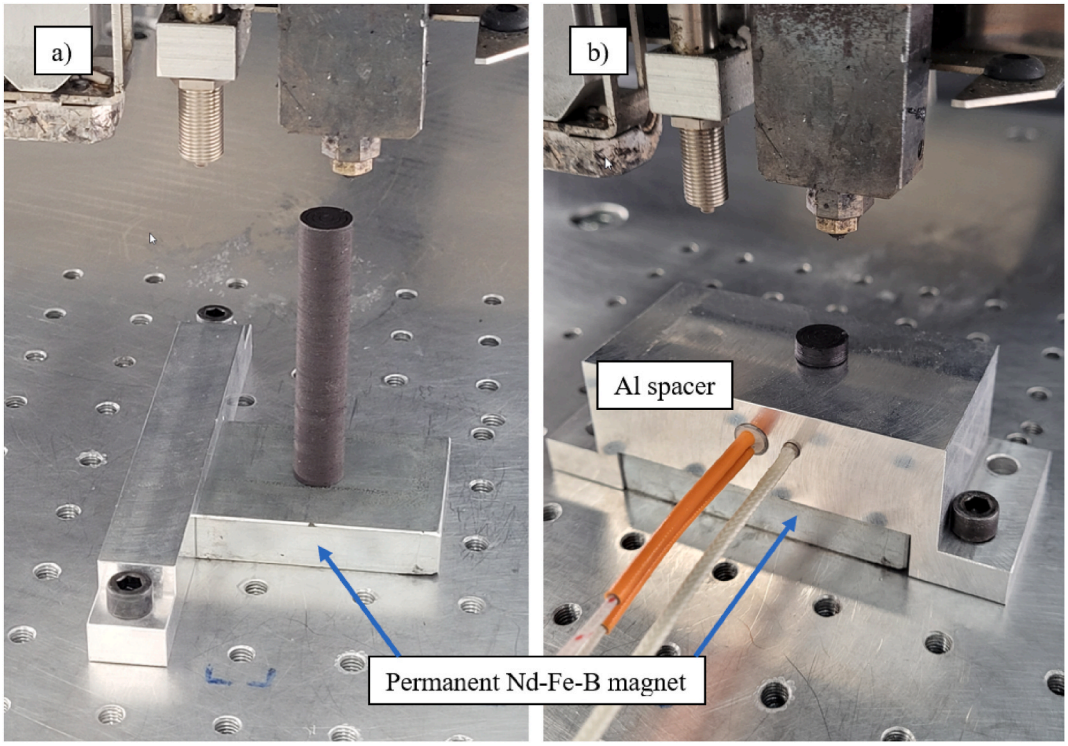


**Fig. 2.** Photographs of the two printing configurations used in this study: (a) continuous printing configuration, where the part is deposited directly on top of a Nd–Fe–B permanent magnet; (b) spacer-based configuration, where non-magnetic aluminium spacers are inserted between the magnet and the print bed to increase the distance from the magnetic field source.

$M_{r,90}$, and intrinsic coercivity $Hc_i$ were obtained.

In the present study, magnetic measurements were performed with the applied field either parallel or perpendicular to the printing direction. The latter coincides with the direction of the external alignment field. Although an additional in-plane direction perpendicular to the filament orientation can be defined, preliminary measurements and the dominance of field-induced alignment justify the use of two orthogonal directions to capture the effective magnetic anisotropy. Possible flow-induced anisotropy effects are therefore implicitly included in the measured response.

The degree of alignment was quantified by the average alignment factor $\langle cos\,\theta \rangle$, which relates the distribution of particle easy-axis orientations to the measured remanence ratio. Following Quispe et al. [33], the alignment factor was calculated from the remanence ratio

$$R = \frac{M_{r,90}}{M_{r,0}} \tag{1}$$

using a relation based on the Fernengel function:

$$\langle cos\,\theta \rangle = cos[arctan(1.7263r)] \tag{2}$$

where $\langle cos\,\theta \rangle = 1$ corresponds to a perfectly aligned system and $\langle cos\,\theta \rangle = 0.5$ to a fully isotropic orientation distribution.

### 2.5. Numerical simulations

Finite element simulations of the magnetic field distribution were performed using the Finite Element Method Magnetics (FEMM) software (version 4.2) [34]. A two-dimensional axisymmetric model was constructed to represent the cylindrical printed sample and the underlying Nd–Fe–B permanent magnet.

The Nd-Fe-B magnet was assigned experimentally determined remanence and coercivity values. The surrounding media (air, aluminium spacer and printed composite) were modelled with appropriate magnetic permeabilities. The $SrFe_{12}O_{19}$–PPS composite was represented as a linear magnetic material with a relative permeability $\mu_r \approx$ 1.2–1.5, corresponding to its partially aligned state and consistent with experimentally observed remanence ratios.

The vertical ($Bz$) and horizontal ($Bx$) components of the magnetic flux density were extracted along the symmetry axis of the cylindrical model. While $Bx$ is strictly zero on the symmetry axis due to axial symmetry, the horizontal field component was evaluated at a small radial offset (r = 0.5 mm) from the axis, corresponding to the interior of the printed cylinder. This approach captures the effective lateral field component experienced by particles away from the ideal symmetry line and allows quantification of field divergence with increasing height. The reported $Bz/Bx$ ratio therefore reflects the local field uniaxiality within the bulk of the printed sample rather than an idealized on-axis value.

## 3. Results

We evaluated the structural and magnetic properties of samples printed at varying distances $h_i$ from the Nd–Fe–B permanent magnet using the two experimental configurations defined in Section 2. As expected, increasing the distance from the magnet resulted in a progressive reduction in both magnetic and structural anisotropy. This behaviour reflects the decreasing influence of the external magnetic field with increasing build height, as the field weakens and becomes less effective in aligning the anisotropic $SrFe_{12}O_{19}$ particles during deposition.

More specifically, the magnetic anisotropy declined due to reduced alignment of the particle easy axes, which manifested as a decrease in remanent magnetization anisotropy and lower values of the alignment factor $\langle cos\,\theta \rangle$. At the same time, structural anisotropy—defined here as the preferred physical orientation of the hexagonal $SrFe_{12}O_{19}$ platelets within the polymer matrix—also decreased, since the weakening magnetic field was no longer sufficient to induce or maintain particle rotation during extrusion. As a result, the microstructure became progressively more isotropic at larger print heights.

A direct comparison between the continuous and spacer-based configurations reveals pronounced differences in how rapidly anisotropy is lost with increasing height. In the continuous configuration, anisotropy persists to substantially larger heights, whereas in the spacer-based configuration it decays much earlier. These trends are quantified through magnetic hysteresis measurements, alignment-factor analysis, and supported by SEM observations, as presented in the following sections.

### 3.1. Magnetic measurements

Magnetic hysteresis measurements were performed to quantify the evolution of anisotropy as a function of print height $h_i$ for both printing configurations. Fig. 3a and b shows the hysteresis curves measured along the magnetic easy axis (0°, parallel to the printing and alignment-field direction) and the hard axis (90°, perpendicular to the printing direction), respectively, for the continuously printed specimen. The curves correspond to individual segments C1–C12, ordered from the segment closest to the Nd–Fe–B magnet (C1, $h_1$ = 2.5 mm) to the topmost segment (C12, $h_{12}$ = 57.5 mm).

The hysteresis curves shown represent the descending branch after saturation; full symmetric loops were measured but are not displayed for clarity, which explains the apparent asymmetry around zero field. This representation allows a clear comparison of remanent magnetization values across different heights.

A pronounced height-dependent trend is observed in the remanent magnetization. Along the easy axis (0°), the remanent magnetization $M_{r,0}$ decreases steadily with increasing height, from 37.8 A $m^2$ $kg^{-1}$ for C1 to 22.3 A $m^2$ $kg^{-1}$ for C12. In contrast, the intrinsic coercivity remains nearly constant across all segments, varying only slightly from 308 kA $m^{-1}$ near the magnet to 298 kA $m^{-1}$ at the highest segment. This indicates that the coercive field is largely unaffected by the alignment conditions during printing, whereas the remanent magnetization is strongly governed by particle orientation.

In the hard-axis (90°) direction, the opposite trend is observed. The remanent magnetization $M_{r,90}$ increases from 7.9 A $m^2$ $kg^{-1}$ for C1 to 20.3 A $m^2$ $kg^{-1}$ for C12. As the easy- and hard-axis remanence values converge with increasing height, the magnetic response transitions progressively from anisotropic to isotropic behaviour. This convergence reflects the gradual loss of preferential alignment of the $SrFe_{12}O_{19}$ particle easy axes as the strength and uniaxiality of the external magnetic field decrease with distance from the magnet.

These trends are summarized in Fig. 4, which shows the remanent magnetization as a function of height for both measurement directions. In the continuous configuration, the decrease in $M_r$, is relatively modest up to approximately 15–17.5 mm (C3–C4), after which the decline becomes more pronounced. Even at the maximum height of 57.5 mm (C12), the easy- and hard-axis curves do not fully overlap, indicating that a small but measurable degree of anisotropy persists throughout the entire print height.

A direct comparison with spacer-based samples ($S_i$) reveals a markedly different behaviour. In the spacer-based configuration, the easy- and hard-axis remanent magnetizations converge at significantly lower heights. The loss of anisotropy occurs at approximately 22.5 mm (S5), beyond which no measurable difference between the two directions is observed. This early convergence demonstrates that, in the absence of an underlying magnetized core, the external magnetic field decays too rapidly with height to sustain particle alignment during deposition.

The evolution of coercivity further supports this interpretation. While the easy-axis coercivity remains nearly constant with height in both configurations, the hard-axis coercivity increases with height in the continuous-print sample, eventually approaching the easy-axis value. This convergence of coercive fields is characteristic of a transition toward magnetic isotropy and mirrors the behaviour observed in the

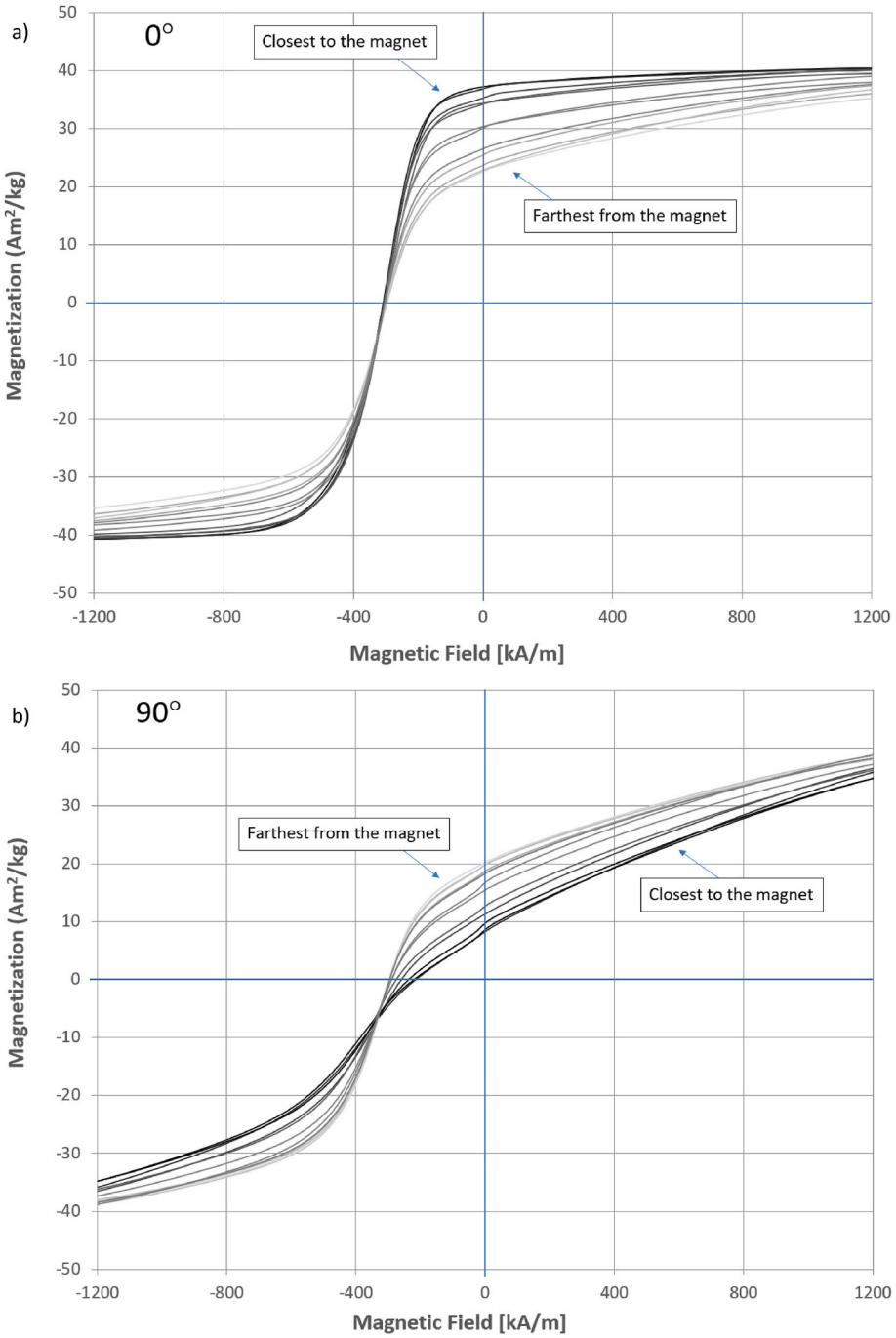


**Fig. 3.** Magnetic hysteresis curves measured along the easy axis (0°, a) and hard axis (90°, b) for the continuously printed specimen. Curves correspond to segments C1–C12 cut at increasing heights from the Nd–Fe–B permanent magnet. Darker curves represent segments closest to the magnet (lower indices), while lighter curves correspond to segments printed at larger heights. The opposite ordering of the curves in panels (a) and (b) reflects the progressive loss of magnetic anisotropy with increasing print height.

remanent magnetization.

Overall, the magnetic measurements clearly demonstrate that printing directly on the permanent magnet significantly extends the height over which magnetic anisotropy can be maintained. The continuously printed material acts as a flux-guiding structure that reinforces the vertical magnetic field component in the upper layers, whereas spacer-based printing lacks this reinforcement and therefore exhibits a much more rapid loss of anisotropy with increasing print height.

The alignment factor $\langle cos\,\theta \rangle$, calculated as described in Section 2.4, provides a compact metric for quantifying the degree of magnetic anisotropy. As shown in Fig. 5, the segment closest to the magnet (C1, h = 2.5 mm) exhibits near-perfect alignment with $\langle cos\,\theta \rangle = 0.94$. In the continuous configuration, high alignment ($\langle cos\,\theta \rangle = 0.94$) is maintained up to approximately 17.5 mm (C4). Beyond this height, the alignment factor decreases gradually, reaching $\langle cos\,\theta \rangle = 0.54$ at the topmost segment (C12, h = 57.5 mm), indicating a significant but not complete loss of anisotropy.

In contrast, spacer-based samples exhibit a much more rapid deterioration in alignment. Already at S2 (7.5 mm), $\langle cos\,\theta \rangle$ decreases substantially, and by approximately 25–27.5 mm (S5–S6) it stabilizes near $\langle cos\,\theta \rangle \approx 0.50 -$ 0.51, corresponding to an effectively isotropic

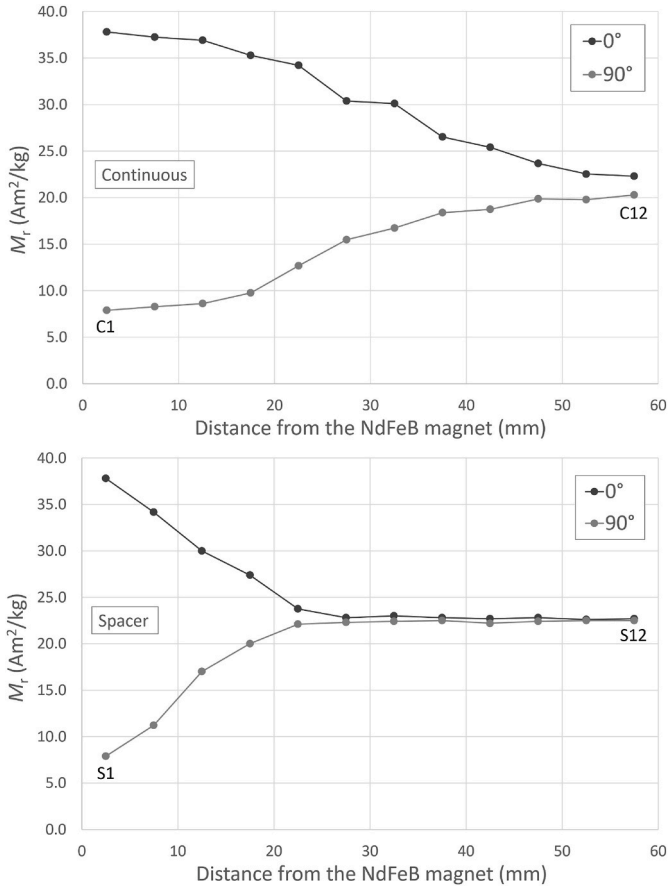


**Fig. 4.** Remanent magnetization $M_r$ as a function of distance from the Nd–Fe–B permanent magnet, measured along the easy axis (0°) and hard axis (90°). Top: Continuous printing configuration, showing data for segments C1–C12. Bottom: Spacer-based printing configuration, showing data for samples $S_i$ printed at corresponding heights. The progressive convergence of the 0° and 90° curves with increasing distance reflects the gradual loss of magnetic anisotropy, which occurs at substantially lower heights in the spacer-based configuration.

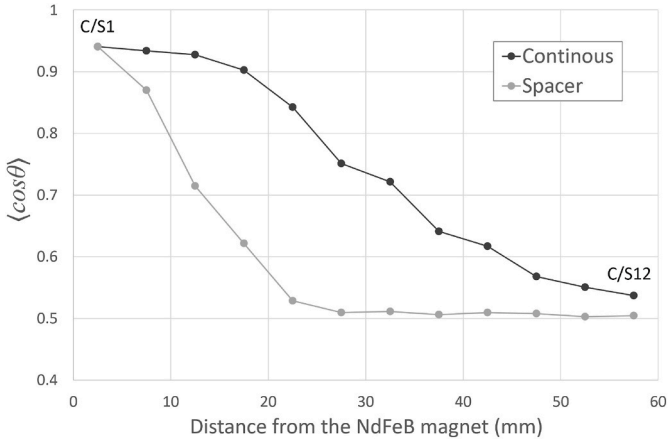


**Fig. 5.** Degree of magnetic alignment ⟨cos θ⟩ as a function of distance from the Nd-Fe-B magnet for both printing configurations: continuous (black) and spacer-based (grey). Alignment remains high in the continuous sample up to ~20 mm, while the spacer sample transitions to isotropy more rapidly, stabilizing near ⟨cos θ⟩ = 0.5.

orientation distribution within experimental resolution. These trends clearly demonstrate the essential role of the magnetized printed material in the continuous configuration, which acts as a flux-guiding core and enables particle alignment to be preserved over substantially larger build heights.

### 3.2. Microstructural analysis

Representative SEM micrographs of cross-sections taken at three characteristic heights—2.5 mm, 22.5 mm, and 57.5 mm—from both printing configurations are shown in Fig. 6. The selected heights correspond to segments C1, C5, and C12 in the continuous configuration and to the corresponding spacer-based samples S1, S5, and S12. These images provide direct evidence of how particle orientation and structural anisotropy evolve with increasing distance from the Nd–Fe–B permanent magnet and therefore reflect the changing local processing conditions experienced during printing.

At the lowest examined height (2.5 mm; C1/S1), both the continuous-print and spacer-based samples exhibit a pronounced directional microstructure. The $SrFe_{12}O_{19}$ particles, which possess a hexagonal platelet morphology, are predominantly oriented with their broad basal planes lying parallel to the x–y plane. Since the magnetic easy axis (c-axis) of the ferrite platelets is perpendicular to the basal plane, this in-plane orientation of the platelet faces indicates that their c-axes are aligned along the vertical direction, coinciding with the direction of the applied magnetic field during printing. This microstructural arrangement reflects strong field-induced rotation of the particles during extrusion and solidification. The excellent alignment observed at this height is fully consistent with the very high magnetic alignment factor measured for C1 ($\langle cos\,\theta \rangle \approx 0.94$) and with the large difference between easy- and hard-axis remanent magnetization reported in Section 3.1.

At the intermediate height of 22.5 mm (C5/S5), clear differences emerge between the two printing configurations. In the continuous configuration (C5), the platelets still exhibit a well-defined preferential orientation. Although local deviations from perfect alignment become more frequent, the majority of particles remain oriented with their basal planes approximately horizontal, indicating that a substantial degree of structural anisotropy persists. This observation is in good agreement with the magnetic measurements, which show that $\langle cos\,\theta \rangle$ remains well above isotropic values at this height and that the remanent magnetization anisotropy is still clearly detectable.

In contrast, the spacer-based specimen at the same height (S5) displays a markedly more disordered microstructure. Platelet orientations are distributed over a wide angular range, and no dominant orientation direction can be identified. This loss of structural alignment correlates directly with the sharp decline in the magnetic alignment factor observed for the spacer-based configuration, in which $\langle cos\,\theta \rangle$ approaches isotropic values (≈0.5) at heights of approximately 25–27.5 mm. The reduced structural anisotropy confirms that, in the absence of a magnetized material beneath the growing part, the external magnetic field decays too rapidly to effectively orient the particles during deposition at this height.

At the highest examined position (57.5 mm; C12/S12), both printing configurations exhibit predominantly random platelet orientations. The $SrFe_{12}O_{19}$ particles are distributed isotropically within the PPS matrix, and the microstructure lacks a clearly preferred alignment direction. This observation is fully consistent with the magnetic measurements, which show that the alignment factor in the continuous configuration decreases to $\langle cos\,\theta \rangle \approx 0.54$ at this height, while the spacer-based configuration remains fully isotropic. Notably, in the continuous-print sample (C12), a faint tendency for platelets to align with their basal planes parallel to the print plane can still be discerned locally, consistent with the small residual anisotropy detected magnetically. In contrast, the spacer-based sample (S12) shows a completely random platelet arrangement without any detectable directional preference.

To aid interpretation of the SEM images, Fig. 7 schematically illustrates the geometry of $SrFe_{12}O_{19}$ hexagonal platelets and the

relationship between platelet orientation and the magnetic easy axis. The easy axis (c-axis) is perpendicular to the flat platelet face; therefore, micrographs in which platelets appear as elongated or broad facets lying in-plane correspond to well-aligned material, whereas micrographs dominated by circular or irregular particle cross-sections indicate increased angular misorientation and reduced anisotropy.

Overall, the SEM analysis provides clear microstructural confirmation of the magnetic trends discussed in Section 3.1. Printing directly on the permanent magnet (continuous configuration) preserves structural anisotropy over a substantially larger height range due to the flux-guiding effect of the magnetized printed material beneath the growing part. In contrast, spacer-based printing leads to an early loss of structural alignment as the magnetic field weakens with increasing distance from the magnet. Together, these observations reinforce the conclusion that the magnitude and directionality of the applied magnetic field, as well as the evolving magnetic properties of the printed material itself, play a decisive role in microstructure development during field-assisted extrusion of ceramic–polymer composites.

### 3.3. Numerical simulations

Numerical simulations of the magnetic field distribution were carried out using the Finite Element Method Magnetics (FEMM) software (version 4.2) [34] to complement and support the experimental observations. A two-dimensional axisymmetric model was constructed to approximate the cylindrical geometry of the printed samples and the underlying Nd–Fe–B permanent magnet. The simulations were designed to replicate the two printing configurations used experimentally: (i) the continuous configuration, in which the printed material is in direct contact with the magnet, and (ii) the spacer-based configuration, in which the printed material is separated from the magnet by non-magnetic aluminium spacers of varying heights.

The Nd–Fe–B magnet was modelled using the experimentally measured remanence and coercivity values. The surrounding regions—air, aluminium spacer, and printed $SrFe_{12}O_{19}$–PPS composite—were assigned appropriate magnetic permeabilities. The composite itself was represented as a homogeneous linear magnetic material with a relative permeability $\mu_r \approx 1.2–1.5$, reflecting its partially aligned magnetic state while keeping the computational model tractable.

Simulations were performed for vertical distances corresponding to

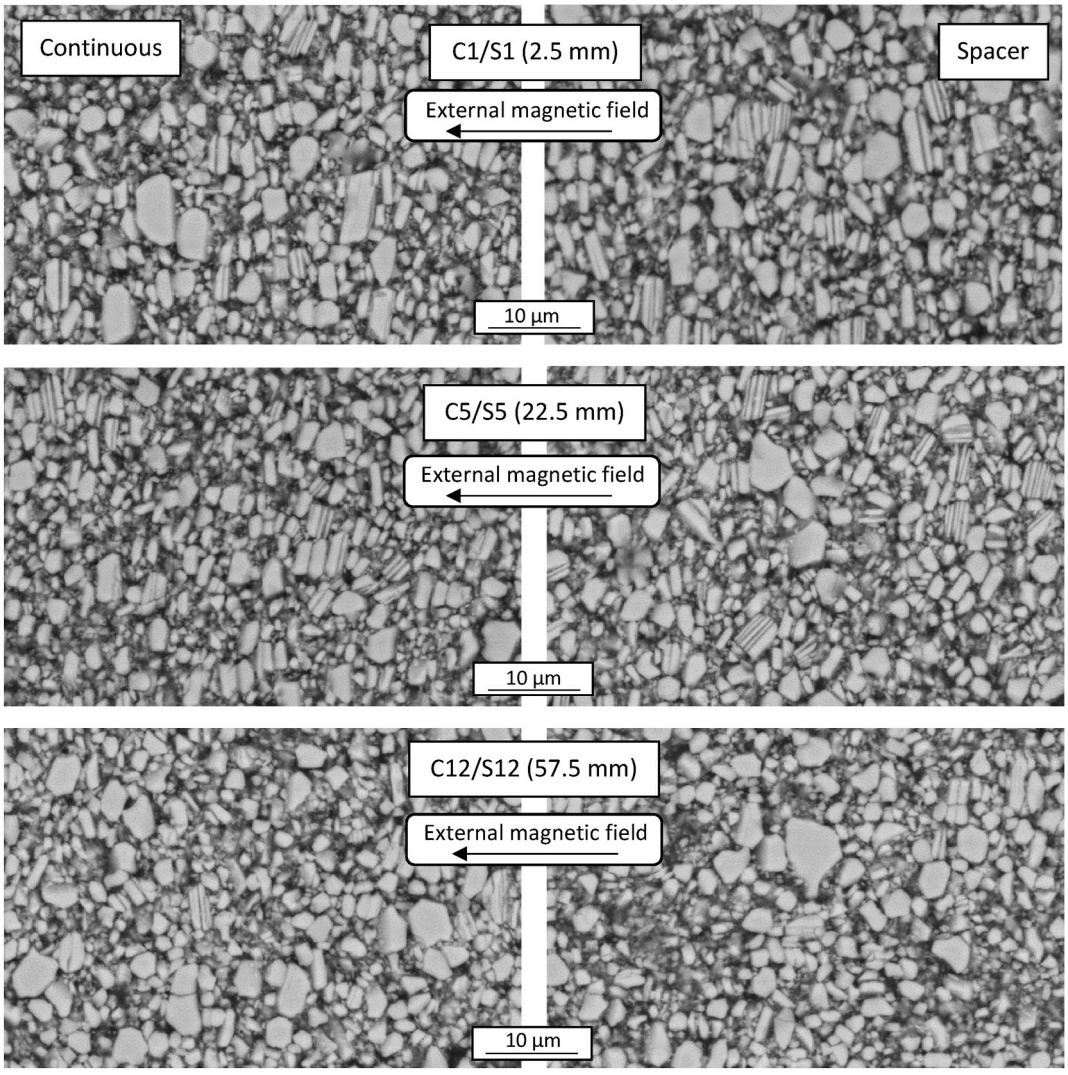


**Fig. 6.** SEM images of cross-sections of the 3D printed magnets at three heights: 2.5 mm (C1/S1), 22.5 mm (C5/S5), and 57.5 mm (C12/S12) from the base. The left column shows samples printed in the continuous configuration, while the right column shows those printed using non-magnetic spacers. A high degree of platelet alignment along the printing (z) direction is evident in the continuous print up to 22.5 mm (C5), gradually deteriorating by 57.5 mm (C12). In contrast, spacer-printed samples show weaker alignment at all heights and become nearly isotropic above 22.5 mm (S5). The images confirm the correlation between structural anisotropy and proximity to the magnetic field source during printing.

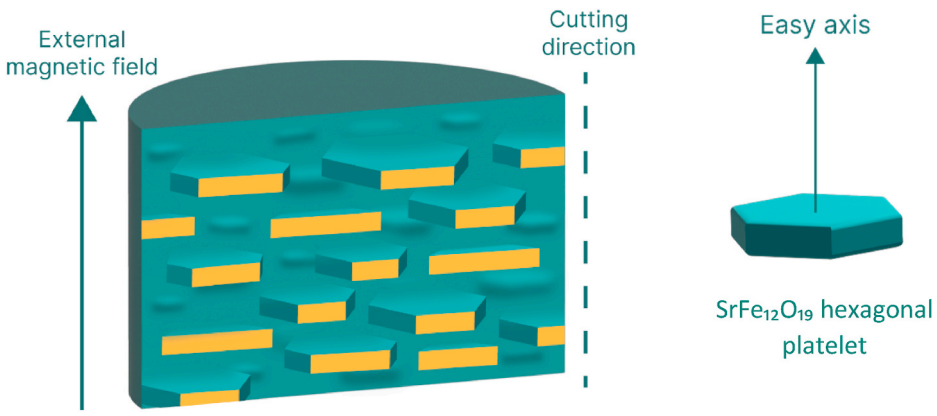


**Fig. 7.** Schematic representation of $SrFe_{12}O_{19}$ hexagonal platelet orientation in a printed sample under an external magnetic field. The left section illustrates aligned particles with their easy axes (c-axes) oriented vertically along the field direction. The cutting direction corresponds to the sample plane used for microstructural SEM analysis. On the right, an individual $SrFe_{12}O_{19}$ hexagonal platelet is shown with its easy axis perpendicular to the flat face, highlighting the direction of preferred magnetization due to magnetocrystalline anisotropy. The dashed line indicates the cutting plane used for SEM analysis. Samples were sectioned parallel to the external magnetic field (build z-direction), i.e., from top to bottom along the cylinder axis.

the same set of heights $h_i$ examined experimentally (C1–C12) and extended by one additional position (C13, h ≈ 62.5 mm) to capture the asymptotic decay of the magnetic field beyond the experimentally accessible print height. For each height, the vertical ($B_z$) and horizontal ($B_x$) components of the magnetic flux density were extracted along the symmetry axis of the cylindrical sample. The anisotropy of the local field was quantified using the ratio $B_z/B_x$, which serves as an indicator of field uniaxiality and directional strength. A high $B_z/B_x$ ratio signifies a predominantly vertical field capable of inducing particle alignment during printing, whereas lower values indicate a more isotropic or laterally diverging field.

Fig. 8 compares the simulated anisotropy ratio $B_z/\ B_x$ with the experimentally measured remanence ratio $M_{r,0}/M_{r,90}$ for both printing configurations. In the continuous configuration, the simulated $B_z/\ B_x$ values remain significantly higher than those of the spacer-based configuration across the entire height range. The gradual decrease in $B_z/B_x$ with increasing distance from the magnet closely follows the trend observed in the magnetic measurements, indicating a progressive loss of field uniaxiality with height. The close correspondence between simulation and experiment confirms that the decay of field directionality is the primary factor governing the reduction of magnetic anisotropy in the printed material.

In the spacer-based configuration, both simulated and experimental results show a much sharper decrease in field anisotropy with height. The vertical component $B_z$ declines rapidly due to the air gap introduced by the spacers, and the horizontal component $B_x$ becomes comparatively more pronounced. As a result, the simulated $B_z/B_x$ values approach unity at much smaller heights than in the continuous configuration, indicating rapid loss of effective alignment capability. This trend closely mirrors the experimental observation that the remanence ratio $M_{r,0}/M_{r,90}$ and alignment factor $\langle cos\ \theta \rangle$ converge toward isotropic values by approximately 22.5–27.5 mm (S5-6) in spacer-based prints.

The simulated magnetic field-line distributions for the two configurations are illustrated schematically in Fig. 9. In the spacer-based setup, the field lines originating from the Nd–Fe–B magnet diverge rapidly into the surrounding air before reaching the printed cylinder, resulting in a

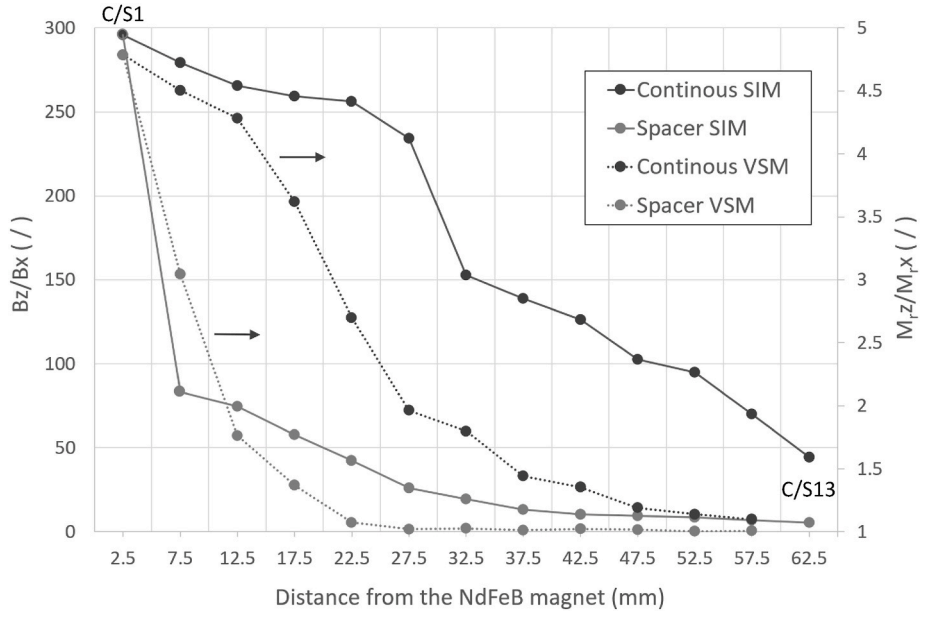


**Fig. 8.** Comparison between simulated magnetic field anisotropy ($B_z/B_x$) and experimental remanent magnetization ratio ($M_{rz}/M_{rx}$) as a function of distance from the Nd–Fe–B magnet (including one simulated position beyond the experimentally measured height). Solid lines show FEMM simulation results for continuous (dark) and spacer (light) setups. Dotted lines with markers show VSM measurements for continuous (black circles) and spacer (grey circles) samples.

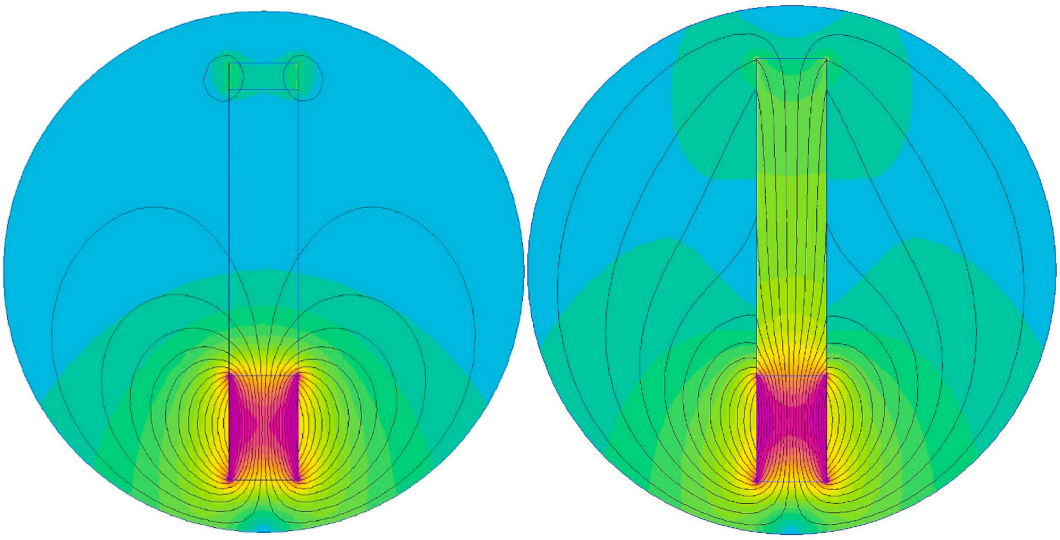

**Fig. 9.** Schematic representation of the magnetic field-line distribution in the two printing configurations investigated in this study. From left to right, the figure shows the spacer-based configuration, where no magnetic material is present between the Nd–Fe–B permanent magnet and the printed part and the magnetic field lines diverge rapidly into the surrounding air, resulting in a weak and non-uniform vertical field within the printed region, and the continuous-print configuration, where the previously deposited $SrFe_{12}O_{19}$–PPS material becomes magnetized during printing and acts as a flux-guiding core, channeling and concentrating the magnetic field into the upper layers of the print and enhancing field strength and uniaxiality.

weak and non-uniform vertical field within the printed region. In contrast, in the continuous-print configuration, the printed $SrFe_{12}O_{19}$–PPS material becomes magnetized during printing and acts as a flux-guiding core. This magnetized region channels and concentrates the magnetic field into the upper layers, enhancing both field strength and uniaxiality in a manner analogous to a ferromagnetic core in an electromagnetic device.

The FEMM simulations therefore validate the hypothesis that the evolving printed composite material actively influences the local magnetic field distribution during printing. By reinforcing the vertical field component and suppressing lateral field divergence, the printed core extends the height over which strongly anisotropic microstructures can be achieved. Conversely, in the absence of such a core—as in the spacer-based configuration—the magnetic field decays too rapidly to sustain particle alignment beyond the lower portion of the print.

Overall, the numerical simulations show strong qualitative agreement with the experimental magnetic measurements and microstructural observations. They confirm that magnetic field decay, field uniaxiality, and the flux-guiding effect of the printed material together determine the achievable anisotropy in field-assisted material-extrusion processing.

## 4. Discussion

The combined magnetic measurements, microstructural observations, and FEMM simulations provide a coherent and self-consistent picture of how anisotropy develops and diminishes during field-assisted material-extrusion processing of $SrFe_{12}O_{19}$–PPS composites. The results demonstrate that the degree of anisotropy achievable in the printed material is governed primarily by the magnitude and uniaxiality of the applied magnetic field—which varies strongly with build height—and by whether the printed material itself contributes to the magnetic flux path during fabrication.

In the continuous-print configuration, printing directly on the Nd–Fe–B permanent magnet leads to magnetization of the initially deposited composite. This magnetized region subsequently acts as a flux-guiding core, concentrating and channeling the external magnetic field into higher layers of the print. As a result, a substantially extended alignment window is achieved. Magnetic measurements show that the remanence anisotropy and alignment factor $\langle \cos\theta \rangle$ remain high up to approximately 15–20 mm from the magnet, with detectable anisotropy persisting even at the maximum investigated height of 57.5 mm. SEM observations corroborate this behaviour, revealing strongly aligned platelet orientations near the base, partially aligned microstructures at intermediate heights, and residual orientation at the top of the sample. FEMM simulations further support this interpretation by showing that the vertical field component remains significantly stronger and more uniaxial in the continuous configuration due to the flux-guiding effect of the printed material.

In contrast, the spacer-based configuration highlights the intrinsic limitations of relying solely on a static permanent magnet located beneath the build platform. Introducing non-magnetic spacers disrupts the flux-guiding pathway, leading to a rapid decay of the vertical magnetic field component and increased divergence of the field lines. Consequently, the alignment factor decreases sharply within the first few millimetres of printing, and by approximately 22.5–27.5 mm the material exhibits magnetically and structurally isotropic behaviour. SEM observations confirm that platelet orientations become essentially random at these heights. These findings emphasize the strong sensitivity of particle alignment to the spatial distribution and directionality of the applied magnetic field.

Together, the two configurations reveal several general principles relevant to field-assisted processing of anisotropic composite materials:

(i) Existence of a finite alignment window.

There exists a characteristic height beyond which the applied magnetic field is no longer sufficient to induce or preserve particle alignment during extrusion. In the present setup, this alignment window extends to approximately 20 mm in the continuous configuration but is substantially shorter in the spacer-based case. This limitation arises directly from the rapid decay of the vertical magnetic field component with distance from the magnet.

(ii) Importance of flux-guiding behaviour in the printed material.

Magnetization of the previously deposited $SrFe_{12}O_{19}$–PPS composite allows it to function analogously to a soft magnetic core, guiding magnetic flux upward and partially compensating for field decay. This self-reinforcing behaviour enhances the local processing conditions and

enables aligned microstructures to form at heights that would otherwise be inaccessible in the presence of an air gap alone. This mechanism is general and may apply to other composite systems containing anisotropic particles with moderate magnetic permeability.

(iii) Coupling between processing conditions and evolving microstructure.

Particle alignment occurs during a limited time window when the material is molten or semi-molten and subject to both magnetic torque and viscous resistance. As the magnetic field weakens with increasing height, the torque becomes insufficient to overcome viscous drag, and platelets progressively solidify in random orientations. The resulting microstructure is then locked in during cooling, such that the local anisotropy reflects the balance between magnetic, thermal, and rheological effects at each print height.

(iv) Implications for scaling and industrial implementation.

For applications requiring anisotropy over larger volumes or build heights, relying on a single permanent magnet beneath the build platform is insufficient. Potential strategies to overcome this limitation include integrating auxiliary magnets or high-permeability inserts within the print, dynamically repositioning the field source during fabrication, employing electromagnets to actively control field strength with height, or tailoring composite rheology to enhance torque-driven particle rotation. Such approaches would enable controlled anisotropy to be maintained over much larger dimensions and facilitate the fabrication of advanced functional components.

(v) General relevance to field-assisted fabrication of anisotropic composites.

Although the present study focuses on $SrFe_{12}O_{19}$–PPS composites, the underlying mechanisms—magnetic field decay, flux guidance by the printed material, competition between magnetic torque and viscous drag, and microstructure lock-in during cooling—are broadly applicable to other ceramic–polymer and particulate composite systems. Similar behaviour can be expected in processes involving electrically conductive platelets, piezoelectric crystallites, or other shape-anisotropic reinforcements, highlighting the general scientific relevance of these findings.

Overall, this discussion demonstrates that anisotropy in field-assisted fused filament fabrication is controlled not only by the externally applied magnetic field but also by the evolving magnetic and rheological properties of the printed material itself. The resulting interaction between field distribution, material response, and processing conditions establishes a self-consistent field–microstructure–property relationship that ultimately governs the performance of the printed composite.

## 5. Conclusions

This study systematically examined the development and limitations of anisotropy in field-assisted material extrusion of $SrFe_{12}O_{19}$–PPS composites using continuous and spacer-based printing configurations. The results demonstrate that anisotropy decreases with increasing print height due to magnetic field decay, as evidenced by the convergence of easy- and hard-axis remanent magnetization and the reduction of the alignment factor $\langle cos\,\theta \rangle$. In the continuous configuration, printing directly on a Nd–Fe–B permanent magnet causes the previously deposited composite to become magnetized and act as a flux-guiding core, maintaining strong particle alignment ($\langle cos\,\theta \rangle > 0.94$) up to approximately 20 mm and measurable anisotropy up to 57.5 mm. In contrast, spacer-based printing lacks this flux-guiding effect, leading to a rapid loss of field uniaxiality and an effectively isotropic microstructure by approximately 22.5–27.5 mm. SEM observations directly corroborate the magnetic measurements, revealing strongly aligned platelets near the magnet, partially aligned structures at intermediate heights, and randomly oriented particles at larger distances. FEMM simulations reproduce these experimental trends and confirm that the extended alignment window in the continuous configuration arises from reinforcement of the vertical magnetic field by the magnetized printed material. Overall, the results establish a clear processing–structure–property relationship for field-assisted extrusion of anisotropic composites and provide practical design guidelines, indicating that preservation of anisotropy over larger build volumes will require flux-guiding strategies or active control of the magnetic field during printing.

## Declaration of competing interest

The authors declare that they have no known competing financial interests or personal relationships that could have appeared to influence the work reported in this paper.

## Acknowledgement

This work is part of the transnational project ADDMAG. The Slovenian part of the project is co-funded by the Ministry of Higher Education, Science and Innovation of the Republic of Slovenia. (Award number: C3330-22-252016)

During the preparation of this work the author used ChatGPT in order to to improve language and readability. After using this tool, the author reviewed and edited the content as needed and takes full responsibility for the content of the publication.

## References

[1] Müller K-H, Sawatzki S, Gauß R, Gutfleisch O. Permanent magnet materials and applications. In: Coey JMD, Parkin SSP, editors. Handbook of magnetism and magnetic materials. Cham: Springer International Publishing; 2021. p. 1369–433. ISBN 978-3-030-63210-6.

[2] McCall SK, Nlebedim IC. Advances in processing, manufacturing, and applications of magnetic materials. JOM 2021;73:3883–4. https://doi.org/10.1007/s11837-021-04979-2.

[3] Gutfleisch O, Willard MA, Brück E, Chen CH, Sankar SG, Liu JP. Magnetic materials and devices for the 21st century: stronger, lighter, and more energy efficient. Adv Mater 2011;23:821–42. https://doi.org/10.1002/adma.201002180.

[4] Périgo EA, Jacimovic J, García Ferré F, Scherf LM. Additive manufacturing of magnetic materials. Addit Manuf 2019;30:100870. https://doi.org/10.1016/j.addma.2019.100870.

[5] Li L, Post B, Kunc V, Elliott AM, Paranthaman MP. Additive manufacturing of near-net-shape bonded magnets: prospects and challenges. Scr Mater 2017;135:100–4. https://doi.org/10.1016/j.scriptamat.2016.12.035.

[6] Paranthaman MP, Shafer CS, Elliott AM, Siddel DH, McGuire MA, Springfield RM, Martin J, Fredette R, Ormerod J. Binder jetting: a novel NdFeB bonded magnet fabrication process. JOM 2016;68:1978–82. https://doi.org/10.1007/s11837-016-1883-4.

[7] Goll D, Vogelgsang D, Pflanz U, Hohs D, Grubesa T, Schurr J, Bernthaler T, Kolb D, Riegel H, Schneider G. Refining the microstructure of Fe-Nd-B by selective laser melting. Phys Status Solidi Rapid Res Lett 2019;13:1800536. https://doi.org/10.1002/pssr.201800536.

[8] Jaćimović J, Binda F, Herrmann LG, Greuter F, Genta J, Calvo M, Tomše T, Simon RA. Net shape 3D printed NdFeB permanent magnet. Adv Eng Mater 2017;19:1700098. https://doi.org/10.1002/adem.201700098.

[9] Huber C, Sepehri-Amin H, Goertler M, Groenefeld M, Teliban I, Hono K, Suess D. Coercivity enhancement of selective laser sintered NdFeB magnets by grain boundary infiltration. Acta Mater 2019;172:66–71. https://doi.org/10.1016/j.actamat.2019.04.037.

[10] Mapley M, Pauls JP, Tansley G, Busch A, Gregory SD. Selective laser sintering of bonded magnets from flake and spherical powders. Scr Mater 2019;172:154–8. https://doi.org/10.1016/j.scriptamat.2019.07.029.

[11] Mapley MC, Tansley G, Pauls JP, Gregory SD, Busch A. Selective laser sintering of bonded anisotropic permanent magnets using an in situ alignment fixture. Rapid Prototyp J 2021;27:735–40. https://doi.org/10.1108/RPJ-09-2020-0220.

[12] Efremov DV, Gerasimova AA. Production of Fe–Cr–Co-based magnets by selective laser sintering. Steel Translat 2021;51:688–92. https://doi.org/10.3103/S0967091221100028.

[13] Goll D, Trauter F, Bernthaler T, Schanz J, Riegel H, Schneider G. Additive manufacturing of bulk nanocrystalline FeNdB based. Micromachines 2021;12:538.

[14] Goll D, Trauter F, Bernthaler T, Schanz J, Riegel H, Schneider G. Additive manufacturing of bulk nanocrystalline FeNdB based permanent magnets. Micromachines 2021;12. https://doi.org/10.3390/mi12050538.

[15] Huber C, Mitteramskogler G, Goertler M, Teliban I, Groenefeld M, Suess D. Additive manufactured polymer-bonded isotropic Ndfeb magnets by stereolithography and their comparison to fused filament fabricated and selective laser sintered magnets. Materials 2020;13. https://doi.org/10.3390/MA13081916.
[16] Lu L, Guo P, Pan Y. Magnetic-field-assisted projection stereolithography for three-dimensional printing of smart structures. J Manuf Sci Eng 2017;139. https://doi.org/10.1115/1.4035964.
[17] Lantean S, Barrera G, Pirri CF, Tiberto P, Sangermano M, Roppolo I, Rizza G. 3D printing of magnetoresponsive polymeric materials with tunable mechanical and magnetic properties by digital light processing. Adv Mater Technol 2019;4:1900505. https://doi.org/10.1002/admt.201900505.
[18] Sonnleitner K, Huber C, Teliban I, Kobe S, Saje B, Kagerbauer D, Reissner M, Lengauer C, Groenefeld M, Suess D. 3D printing of polymer-bonded anisotropic magnets in an external magnetic field and by a modified production process. Appl Phys Lett 2020;116:092403. https://doi.org/10.1063/1.5142692.
[19] Huber C, Abert C, Bruckner F, Groenefeld M, Muthsam O, Schuschnigg S, Sirak K, Thanhoffer R, Teliban I, Vogler C, et al. 3D print of polymer bonded rare-earth magnets, and 3D magnetic field scanning with an end-user 3D printer. Appl Phys Lett 2016;109:162401. https://doi.org/10.1063/1.4964856.
[20] Podmiljšak B, Kobe S, Tomše T, Bek M, Kotnik T, Slemenik Perše L, Žagar E, Saje B, Žužek K, Šturm S. Additive-manufactured anisotropic magnets for harsh environments. J Magn Magn Mater 2023;586:171165. https://doi.org/10.1016/j.jmmm.2023.171165.
[21] Paranthaman MP, Yildirim V, Lamichhane TN, Begley BA, Post BK, Hassen AA, Sales BC, Gandha K, Nlebedim IC. Additive manufacturing of isotropic NdFeB PPS bonded permanent magnets. Materials 2020;13. https://doi.org/10.3390/ma13153319.
[22] Slapnik J, Pulko I, Rudolf R, Anžel I, Brunčko M. Fused filament fabrication of Nd-Fe-B bonded magnets: comparison of PA12 and TPU matrices. Addit Manuf 2021;38:101745. https://doi.org/10.1016/j.addma.2020.101745.
[23] Palmero EM, Rial J, de Vicente J, Camarero J, Skårman B, Vidarsson H, Larsson P-O, Bollero A. Development of permanent magnet MnAlC/Polymer composites and flexible filament for bonding and 3D-Printing technologies. Sci Technol Adv Mater 2018;19:465–73. https://doi.org/10.1080/14686996.2018.1471321.
[24] Xu Z, Chen F, Wang X, Chen K, Tang Z, Bo X, Jiang S. Effect of NdFeB particle size on the performance of 3D printed bonded magnets of polyamide-based composites. Polym Compos 2022;43:8368–76. https://doi.org/10.1002/pc.27007.
[25] Zhang X, Hu H, Tang D, Zhang C, Fu J, Zhao P. Magnetic flexible tactile sensor via direct ink writing. Sensor Actuator Phys 2021;327:112753. https://doi.org/10.1016/j.sna.2021.112753.
[26] Brown D, Ma B-M, Chen Z. Developments in the processing and properties of NdFeb-Type permanent magnets. J Magn Magn Mater 2002;248:432–40. https://doi.org/10.1016/S0304-8853(02)00334-7.
[27] Liu XB, Kesler MS, Besser MF, Kramer MJ, McGuire MA, Nlebedim IC. Effect of processing hydrogen pressure on magnetic properties of HDDR Nd-Fe-B magnet. IEEE Trans Magn 2021;57:1–4. https://doi.org/10.1109/TMAG.2020.3022739.
[28] Sarkar A, Paranthaman MP, Nlebedim IC. In-Situ magnetic alignment model for additive manufacturing of anisotropic bonded magnets. Addit Manuf 2021;46:102096. https://doi.org/10.1016/j.addma.2021.102096.
[29] Erokhin S, Berkov D. Mechanical orientation of fine magnetic particles in powders by an external magnetic field: simulation-based optimization. Phys Status Solidi (b) 2020;257:2000404. https://doi.org/10.1002/pssb.202000404.
[30] Gandha K, Li L, Nlebedim IC, Post BK, Kunc V, Sales BC, Bell J, Paranthaman MP. Additive manufacturing of anisotropic hybrid NdFeB-SmFeN nylon composite bonded magnets. J Magn Magn Mater 2018;467:8–13. https://doi.org/10.1016/j.jmmm.2018.07.021.
[31] Suppan M, Huber C, Mathauer K, Abert C, Brucker F, Gonzalez-Gutierrez J, Schuschnigg S, Groenefeld M, Teliban I, Kobe S, et al. In-Situ alignment of 3D printed anisotropic hard magnets. Sci Rep 2022;12:17590. https://doi.org/10.1038/s41598-022-20669-8.
[32] Schäfer K, Fim RGT, Maccari F, Braun T, Riegg S, Skokov KP, Koch D, Bruder E, Radulov I, Ahrens CH, et al. Laser powder bed fusion of anisotropic Nd-Fe-B bonded magnets utilizing an in-Situ mechanical alignment approach. J Magn Magn Mater 2023;583:171064. https://doi.org/10.1016/j.jmmm.2023.171064.
[33] Quispe LT, Röhrig M, Monteiro JL, Lopes LU, Wendhausen PA. Fast experimental estimation of texture distribution and alignment degree in permanent magnets. J Appl Phys 2020;128:165101. https://doi.org/10.1063/5.0028005.
[34] Meeker D. Finite element method magnetics. Available online: https://www.femm.info/wiki/HomePage.